Journal of Magnetic Resonance 208 (2011) 284–290

Contents lists available at ScienceDirect

Journal of Magnetic Resonance

journal homepage: www.elsevier.com/locate/jmr

Communication

Gradient-induced longitudinal relaxation of hyperpolarized noble gases in the fringe fields of superconducting magnets used for magnetic resonance

Wangzhi Zheng [a], Zackary I. Cleveland [b], Harald E. Möller [c], Bastiaan Driehuys [b,*]

[a] Triangle Universities Nuclear Laboratory and Department of Physics, Duke University, Durham, NC 27708, USA
[b] Center for In Vivo Microscopy, Department of Radiology, Duke University Medical Center, Durham, NC 27710, USA
[c] Max Planck Institute for Human Cognitive and Brain Sciences, Stephanstr. 1a 04103 Leipzig, Germany

ARTICLE INFO

Article history:
Received 15 September 2010
Revised 9 November 2010
Available online 4 December 2010

Keywords:
Longitudinal relaxation
Hyperpolarized
^{3}He
^{129}Xe
Nuclear magnetic resonance
Magnetic resonance imaging
Superconducting magnet
Magnetic field gradient

ABSTRACT

When hyperpolarized noble gases are brought into the bore of a superconducting magnet for magnetic resonance imaging (MRI) or spectroscopy studies, the gases must pass through substantial field gradients, which can cause rapid longitudinal relaxation. In this communication, we present a means of calculating this spatially dependent relaxation rate in the fringe field of typical magnets. We then compare these predictions to experimental measurements of ^{3}He relaxation at various positions near a medium-bore 2-T small animal MRI system. The calculated and measured relaxation rates on the central axis of the magnet agree well and show a maximum ^{3}He relaxation rate of $3.83 \times 10^{-3}\ s^{-1}$ ($T_1 = 4.4$ min) at a distance of 47 cm from the magnet isocenter. We also show that if this magnet were self-shielded, its minimum T_1 would drop to 1.2 min. In contrast, a typical self-shielded 1.5-T clinical MRI scanner will induce a minimum on-axis T_1 of 12 min. Additionally, we show that the cylindrically symmetric fields of these magnets enable gradient-induced relaxation to be calculated using only knowledge of the on-axis longitudinal field, which can either be measured directly or calculated from a simple field model. Thus, while most MRI magnets employ complex and proprietary current configurations, we show that their fringe fields and the resulting gradient-induced relaxation are well approximated by simple solenoid models. Finally, our modeling also demonstrates that relaxation rates can increase by nearly an order of magnitude at radial distances equivalent to the solenoid radius.

1. Introduction

Magnetic resonance imaging (MRI) and nuclear magnetic resonance (NMR) spectroscopy using the hyperpolarized (HP) gases ^{3}He and ^{129}Xe have emerged as important techniques for studying lung function [1] with additional applications in areas such as imaging the brain, the development of biosensors [2], and materials science [3,4]. Hyperpolarized gases deliver large MR signals by virtue of their high nuclear spin polarizations, which are typically orders of magnitude greater than those attainable at thermal equilibrium. Since the degree of nuclear spin alignment drives the signal-to-noise ratio (SNR) of the images and spectra, extraordinary efforts have been applied to increase the nuclear polarization. Key steps have included the development of spectrally narrowed high-power lasers [3], the introduction of spin-exchange optical pumping (SEOP) using alkali metal hybrids [4,5], and the development of large-scale ^{129}Xe polarizers [6]. In recent years, polarization levels as high as 81% have been reported for ^{3}He [7], and 64% has been reported for ^{129}Xe produced in volumes of several liters [6].

Relative to increasing polarization, less attention has been applied to retaining the hard-won polarization until it can be used. Once the polarization process is stopped, the nuclei will inevitably relax back to their thermal equilibrium state, where polarization is negligible. Therefore, it is the degree of polarization that is actually delivered to the objects under study that is ultimately important. Hence, every effort must also be made to ensure that longitudinal relaxation is as slow as possible. Unlike the radioactive decay of nuclear isotopes, which is characterized by well-defined half-lives, the longitudinal relaxation time (T_1) of noble gases can vary massively, ranging from hundreds of hours for ^{3}He [7] to only a few seconds [8].

The mechanisms driving T_1 relaxation can be broadly characterized as intrinsic relaxation, which cannot be avoided, and extrinsic relaxation, which can, in principle, be engineered to become negligible, but in practice dominates the signal loss. Intrinsic relaxation of ^{3}He is driven by the dipole–dipole interaction during collisions with other ^{3}He atoms and has been shown theoretically by Newbury et al. to give a T_1 of ~744 h-amg (an amagat is the density of 1 atm of gas at 273 K) [9]. Intrinsic relaxation for ^{129}Xe, which

* Corresponding author. Address: Center for In Vivo Microscopy, Box 3302, Duke University Medical Center, Durham, NC 27710, USA. Fax: +1 919 684 7122.
E-mail address: bastiaan.driehuys@duke.edu (B. Driehuys).

1090-7807/$ - see front matter © 2010 Elsevier Inc. All rights reserved.
doi:10.1016/j.jmr.2010.11.006

is driven by the spin-rotation interactions [10] and chemical shift anisotropy [11] caused by binary collisions and the formation of transient Xe–Xe van der Waals molecules [12], has been shown by Chann et al. to provide a T_1 of 4.1 h at 1 amg [13].

The extrinsic relaxation mechanisms include relaxation resulting from collisions with paramagnetic atoms [14,15] such as O_2, collisions with surfaces, relaxation induced by electromagnetic noise, and diffusion through magnetic field gradients [16]. Oxygen-induced relaxation is well understood, contributing a room temperature T_1 of 2.23 s-amg for ^{3}He [15] and 2.03 s-amg for ^{129}Xe [14]. Despite its potent relaxivity, the effects of oxygen can be readily reduced to negligible levels by appropriate evacuation and/or purging of vessels in which HP gases are to be stored [17]. Moreover, surface-induced relaxation, while still not fully understood, has been effectively mitigated. ^{3}He relaxation in glass cells coated with alkali metals, is now characterized by T_1 values exceeding hundreds of hours [7], even enabling HP ^{3}He to be produced centrally and shipped all over the globe [18].Wall relaxation of ^{129}Xe has also been reduced to an extraordinary extent with a recent report of $T_1^W = 176$ h in high magnetic fields [19].

However, of specific importance to MRI and NMR applications of HP gases is their relaxation in the strong external transverse magnetic field gradient that leads from the periphery of the superconducting magnet into its isocenter. In all high-field experiments, HP gases must be transported from the low-field region outside the magnet, where they are produced to the high-field detection region within the magnet. This necessitates passing through strong magnetic field gradients. Although gradient-induced relaxation has been well studied [16] and can be made negligible in homogeneous fields such as Helmholtz pairs, solenoids, or even magnetostatic cavities [20], this mechanism has not been considered for the regions peripheral to these magnet structures. The effect is of obvious importance for clinical studies, where the ^{3}He or ^{129}Xe must pass through external gradient to be delivered to the patient. It can have an even greater impact in small animal imaging studies, where HP gases are typically delivered over an extended period of several minutes [21], during which gradient-induced relaxation can dramatically depolarize the gas in the reservoir residing in the fringe field of the magnet [22]. In addition to reducing SNR, this unwanted relaxation complicates the interpretation of experiments—for example, in regional ventilation measurements [23] that rely on the magnitude of the HP signal for quantification.

The aim of this manuscript is to calculate the external field inhomogeneity of a variety of scanner designs, predict the induced relaxation rates, and identify the spatial locations, where this effect is of greatest concern. We validate the calculations by comparing predicted and observed ^{3}He relaxation rates for a specific magnet geometry we routinely employ for small animal HP gas MRI. Finally, because most MRI magnet designs are complex and proprietary, we also show a means to make practical estimates of the gradient-induced T_1 in the vicinity of a clinical scanner, without requiring exact knowledge of the current configuration in magnet. We demonstrate that, even when extended to a more complicated self-shielded clinical magnet, the calculated relaxation rate predicted using our simplified model agrees well with the rate predicted using the more complicated exact current configuration.

2. Theory

The longitudinal relaxation rate of HP gases induced by diffusion through transverse magnetic field gradients, $1/T_1^G$, can be expressed as [16]

$$\frac{1}{T_1^G} = D\frac{|\vec{\nabla}B_x|^2 + |\vec{\nabla}B_y|^2}{B_0^2}\frac{1}{1+(\omega_0\tau_c)^2}, \tag{1}$$

where $|\vec{\nabla}B_x|^2$ is defined as $(\partial B_x/\partial x)^2 + (\partial B_x/\partial y)^2 + (\partial B_x/\partial z)^2$, D is the diffusion constant of HP gas, ω_0 is the nuclear resonance frequency at the static magnetic field strength, B_0, and the relevant correlation time, τ_c, is approximately the mean time between HP gas collisions. As first explained by Gamblin and Carver [24], it is the diffusion of gas atoms through the gradients of the transverse magnetic fields $|\vec{\nabla}B_x|^2$ and $|\vec{\nabla}B_y|^2$ that causes relaxation. In the atoms' reference frame, their random Brownian motion causes the gradients to appear as randomly fluctuating transverse magnetic fields, which can induce spin flips just as a transverse radio frequency pulse would. For common situations Eq. (1) is amenable to several simplifications. Firstly, the last term approaches unity under low-field conditions, an assumption which is valid for ^{3}He under our experimental conditions (it is 0.99 at 2 T), given correlation times of 0.29 ns at 300 K for 1 atm [25]. Secondly, since typical superconducting MR magnets possess cylindrical symmetry, i.e. an azimuthally symmetric current distribution, the polar component of the field B_ϕ is explicitly zero, leaving the only non-trivial components B_z, where $\hat{z}$ lies along the central axis of the field, and B_ρ, where $\hat{\rho}$ is the radial component, which is perpendicular to the central axis. Moreover, the azimuthally symmetric current distribution assures that $B_z(\rho, Z)$ and $B_\rho(\rho, z)$ are functions only of ρ and z and do not depend on ϕ. For this type of symmetry, as we show in Appendix A, it is possible to transform $|\vec{\nabla}B_x|^2 + |\vec{\nabla}B_y|^2$ in Eq. (1) into cylindrical form with $|\vec{\nabla}B_\rho|^2 + B_\rho^2/\rho^2$, and Eq. (1) can be rewritten as

$$\frac{1}{T_1^G} = D\frac{|\vec{\nabla}B_\rho|^2 + B_\rho^2/\rho^2}{B_0^2}. \tag{2}$$

2.1. On-axis relaxation rate

While relaxation anywhere near the superconducting magnet is potentially important, useful insights can be gained by first considering only the relaxation behavior along the z-axis. For our case of azimuthal symmetry, $|\vec{\nabla}B_\rho|^2 = |\partial B_\rho/\partial\rho|^2$, because B_ρ is zero on-axis, and thus has no non-zero z-derivative along the z-axis. Moreover, as $\rho \to 0$, $B_\rho/\rho \to \partial B_\rho/\partial\rho$, and we can exploit the divergence-free nature of the magnetic field ($\vec{\nabla}\cdot\vec{B} = 0$) to relate the ρ and z-derivatives. For azimuthal symmetry and $B_\phi = 0$, only two terms of the divergence equation are non-zero giving

$$\vec{\nabla}\cdot\vec{B} = \frac{1}{\rho}\frac{\partial}{\partial\rho}(\rho B_\rho) + \frac{\partial}{\partial z}B_z = 0, \tag{3}$$

which yields the relationship $\partial B_\rho/\partial\rho = -\frac{1}{2}\partial B_z/\partial z$. Making this substitution into Eq. (2) gives us, for the case of $\rho = 0$, the gradient-induced relaxation rate in terms of only B_z and its z-derivative

$$\frac{1}{T_1^G} = \frac{D}{2}\left(\frac{\partial}{\partial z}B_z^{(0)}(0,z)\right)^2 \Big/ (B_z(0,z))^2. \tag{4}$$

2.2. Off-axis relaxation rates

Considering relaxation off-axis for small values of ρ (i.e., near the central axis), we show through symmetry arguments already outlined and further approximations detailed in Appendix B that it is possible to express both B_ρ and B_z in terms of only B_z and its derivatives as

$$B_z(\rho,z) \simeq B_z(0,z) - \frac{\rho^2}{4}\frac{\partial^2}{\partial z^2}B_z(0,z), \tag{5a}$$

$$B_\rho(\rho,z) \simeq -\frac{\rho}{2}\frac{\partial}{\partial z}B_z(0,z) + \frac{\rho^3}{16}\frac{\partial^3}{\partial z^3}B_z(0,z). \tag{5b}$$

These relations make it possible to extend beyond Eq. (4) and account for relaxation near the central axis. Substituting Eqs. (5a)

and (5b) into Eq. (2) and making the near-axis approximation $B_0 \approx B_z$ yields

$$\frac{1}{T_1^G} \approx D\left[\left(\frac{-1}{2}\frac{\partial}{\partial z}B_z(0,z)+\frac{3\rho^2}{16}\frac{\partial^3}{\partial z^3}B_z(0,z)\right)^2 + \left(\frac{-\rho}{2}\frac{\partial^2}{\partial z^2}B_z(0,z)+\frac{\rho^3}{16}\frac{\partial^4}{\partial z^4}B_z(0,z)\right)^2 + \left(\frac{-1}{2}\frac{\partial}{\partial z}B_z(0,z)+\frac{\rho^2}{16}\frac{\partial^3}{\partial z^3}B_z(0,z)\right)^2\right] \Big/ \left(B_z(0,z)-\frac{\rho^2}{4}\frac{\partial^2}{\partial z^2}B_z(0,z)\right)^2. \quad (6)$$

Note that this expression, in the limit $\rho \to 0$, reduces to the simple on-axis result given in Eq. (4).

The exact form of $B_z(0, z)$ depends on the geometry of the magnet and can be difficult to obtain in analytical form for complex or proprietary magnet designs. However, a remarkable feature of Eqs. (5a) and (5b), which relate the off-axis field and the on-axis field, is that one can predict the field off-axis without knowing the exact current configuration that gives rise to $B_z(0, z)$. In fact, any formula that adequately captures the behavior of the on-axis magnetic field can be used to predict the field off-axis through Eqs. (5a) and (5b). This gives us freedom to choose a reasonably simple functional form to describe the magnetic field and use this to calculate the longitudinal relaxation rate in the near-axis region. In our studies, we have found that a simple solenoid model is sufficient to approximate the observed on-axis fringe field in our superconducting MR magnet, with $B_z(0, z)$ given by

$$B_z(0,z) = A\left(\frac{L/2+z}{\sqrt{R^2+(L/2+z)^2}}+\frac{L/2-z}{\sqrt{R^2+(L/2-Z)^2}}\right), \quad (7)$$

where L is the length of the solenoid, R is the radius of the solenoid, and A is the factor proportional to the current density in the solenoid. Substituting Eq. (7) into Eqs. (4) and (6) yields the longitudinal relaxation rate $1/T_1^G$ on the axis and in the near-axis region, respectively.

3. Experimental methods

3.1. Hyperpolarization methods

Hyperpolarized ^{3}He (99.999% pure, Spectra Gases Inc., Alpha, NJ) was prepared for relaxation measurements by spin-exchange optical pumping [26]. ^{3}He was polarized overnight to 30–40% using a prototype commercial polarizer (model 9800, MITI, Durham, NC). Prior to relaxation experiments, the spin-exchange optical cell was cooled to room temperature, and ~100 ml of HP ^{3}He was dispensed into 8 × 10 cm^2 Tedlar bags (Jensen Inert Products, Coral Springs, FL) at atmospheric pressure.

3.2. Magnetic field mapping

Magnetic field mapping and relaxation measurements were made for a 2-T horizontal bore magnet (Oxford Instruments, Oxford, UK) with a 30-cm bore. Its magnetic field was measured along the central axis (i.e., z-axis) and 11.4-cm off-axis using a gauss-meter (Model 5080 F.W. Bell, Orlando, FL). The on-axis field has only an axial component ($\hat{z}$), whereas the off-axis field has both axial ($\hat{z}$) and radial ($\hat{\rho}$) components. The measured on-axis magnetic field data were fit using a non-linear least squares algorithm to the solenoid model in Eq. (7) to determine the values of A, L, and R that best described the magnet (see Table 1). These values were then used in conjunction with Eqs. (5a) and (5b) to predict both the longitudinal and transverse components of the field 11.4-cm off-axis and these predictions were compared with the field measurements (see Fig. 1).

3.3. HP ^{3}He T_1 measurements

Inhomogeneity-induced relaxation is expected to be largest for ^{3}He compared with other noble gases given its sizeable free diffusion coefficient (~2 cm^2/s at one atmosphere and room temperature). Therefore, ^{3}He was used to measure the position-dependent relaxation time in the vicinity of the 2-T magnet. Prior to starting the relaxation measurements, the ^{3}He NMR signal was measured in the Tedlar bag using a low-field polarimeter for HP gases [27]. The polarimeter had a holding field of 7 Gauss provided by a pair of Helmholtz coils with a radius of 30 cm.

The T_1 of HP ^{3}He as a function of the distance from the center of the superconducting magnet isocenter was made by shuttling the ^{3}He bag to the position of interest, leaving it to relax for a fixed period of time, and returning to the measurement station to record the NMR signal. This was repeated several times to obtain a complete T_1 decay curve at each position. For a typical experiment, it took ~10 s to move the bag from the polarimeter to the relaxation position, where the bag was left for exactly 30 s. These steps were repeated five times for a given location in the fringe field region. The time spent in shuttling the bag (~10 s) and on the measurement station (~10 s) was ignored because the relaxation during these time periods is negligible compared with that experienced in the strong field gradients near the magnet.

Prior to fitting the NMR signals to determine a T_1 for each position, the data were corrected for the small amount of polarization lost due to application of the RF pulses used for measuring polarization. The loss factor was determined by taking 10 successive polarization measurements with 1 s intervals to minimize the effect of wall relaxation. The resulting polarization values were then fit to the functional form $P(n) = P_0 f^n$, where P_0 is the initial polarization, f is the fractional polarization remaining after each pulse, and n is the index of the measurement number. Since the measured T_1 is sensitive to f, four sets of loss factor measurements were carried out and resulted in an average retained fraction, $\bar{f} = 0.9797 \pm 0.0033$. The T_1 at each location was obtained by using a modified exponential decay function to fit the measurement to

$$S(n) = S_0 \exp\left(-\frac{nT_R}{T_1}\right)\bar{f}^{2n}, \quad (8)$$

where T_R = 30 s is the time the bag spent in the relaxation position. The loss due to the RF pulse for each time point is $\bar{f}^2$ because two consecutive polarization measurements were taken for each time point. The uncertainty from the measured $\bar{f}$ dominates the error in T_1 over all other uncertainties in our experiments, such as the fitting error and the dimension of the Tedlar bag.

The measured relaxation time described above consists of three mechanisms—wall relaxation T_1^W, magnetic field gradient-induced relaxation T_1^G, and the intrinsic ^{3}He–^{3}He relaxation T_1^{int} given by

$$\frac{1}{T_1} = \frac{1}{T_1^W}+\frac{1}{T_1^G}+\frac{1}{T_1^{\text{int}}}. \quad (9)$$

The intrinsic ^{3}He–^{3}He dipole relaxation is on the order of 1 month and can be ignored. The wall relaxation T_1^W was determined with the bag in the polarimeter (where T_1^G was negligible) and measured to be 5125 ± 264 s. This provided only a minor correction to the measured relaxation times.

Table 1
Parameters used to characterize the fringe field.

	Primary Solenoid			Shielding Solenoid[a]		
	L (cm)	R (cm)	A (T)	L_s (cm)	R_s (cm)	A_s (T)
2-T unshielded [b]	75.0 ± 0.1	22.2 ± 0.1	1.2707	N/A	N/A	N/A
2-T shielded [b]	75.0 ± 0.1	22.2 ± 0.1	1.74	100	35	−0.493
1.5-T shielded [c]	174.5 ± 0.1	39.2 ± 0.1	1.745	284.5 ± 0.1	131.7 ± 0.1	−0.04708

[a] Subscript *s* refers to values for the reversed solenoid used to model the self-shielded configuration.
[b] Values are based on best fits of the measured on-axis field.
[c] Values are based on best fits of the solenoid model to the exact current configuration of the magnet ranging from 50 cm to 300 cm.

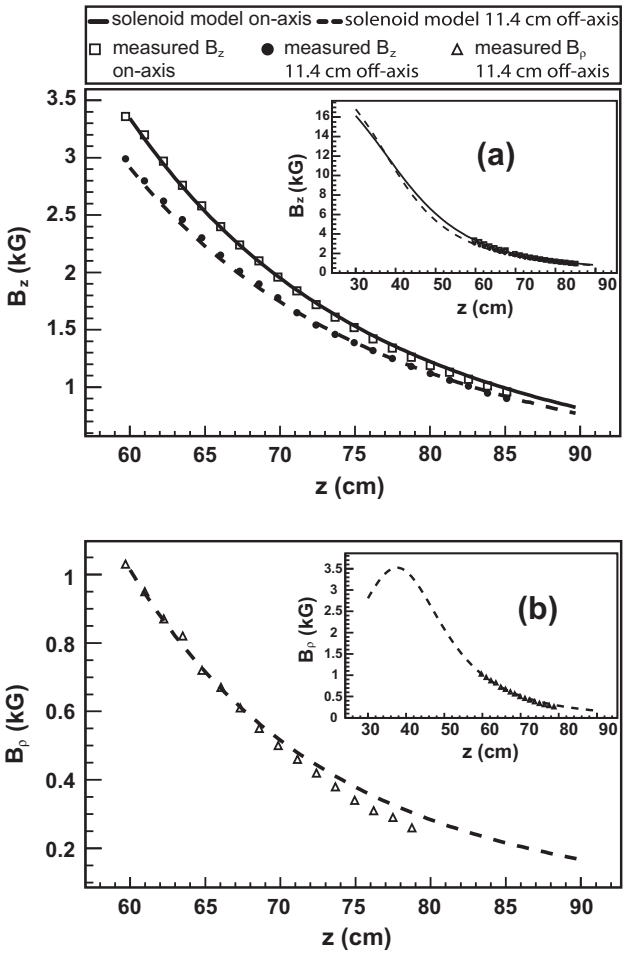

Fig. 1. Spatial dependence of the fringe magnetic field of the 2-T superconducting magnet. The experimentally measured fringe field is well described by a simple solenoid with radius $R = 22.2$ cm and length $L = 75.0$ cm. Here, $z = 0$ represents the center of the magnet. The insets show the same curves enlarged to cover the range considered in the relaxation rate measurements. (a) Spatial variation in B_z. (b) Spatial variation in B_ρ. Because the on-axis field does not have a ρ component, only the field 11.4 cm off-axis is shown.

4. Results and discussion

The fringe magnetic field measured on-axis for the 2-T magnet is compared to the field calculated using the solenoid model and plotted in Fig. 1. The calculated on-axis field best approximates the measured one using $L = 75.0 \pm 0.1$ cm and $R = 22.2 \pm 0.1$ cm for the length and radius of the solenoid (see Table 1). Fig. 1a shows clearly that Eqs. (5a) and (5b) in conjunction with the simple solenoid model predict the z component of the off-axis fringe field well. Applying the same model to predict the ρ component of the off-axis fringe field again (Fig. 1b) shows good agreement, except that the measured field begins to deviate from the predicted function at about $z = 75$ cm. This could indicate that the approximations used to arrive at Eq. (5) are not fully valid this far off-axis or may reflect the limitations of this simple solenoid model at large z or r. Nonetheless, the agreement between measured and calculated fields is sufficiently good to suggest that the solenoid model will be adequate for calculating the inhomogeneity-induced relaxation rate of this magnet geometry.

The solenoid model is used in conjunction with on-axis Eq. (4) to calculate the longitudinal relaxation rate $1/T_1^G$ of ^{3}He in the fringe field of the magnet. The prediction is plotted as a solid line in Fig. 2, along with data points representing the experimentally determined values of $1/T_1^G$. The measured values of $1/T_1^G$ show a maximum rate of $3.83 \times 10^{-3}\ s^{-1}$ at $z = 47$ cm from the magnet isocenter, which is in good agreement with the maximum rate of $3.71 \times 10^{-3}\ s^{-1}$ at $z_{max} = 51.0$ cm predicted by the solenoid model. The predicted position of maximum relaxation is 4 cm off from the measured one; however, the size of this discrepancy is smaller than the dimensions of the Tedlar bag, making this difference understandable. In fact, the measured $1/T_1^G$ is in excellent agreement with predictions at all positions.

Given the good agreement between theory and measurement for one specific magnet design, it is reasonable to apply this modeling approach to other magnet configurations. In recent years, self-shielded (actively-shielded) magnet designs have gained increasing prominence in NMR and MRI. These designs generate a field that rolls off rapidly with distance and are therefore, likely

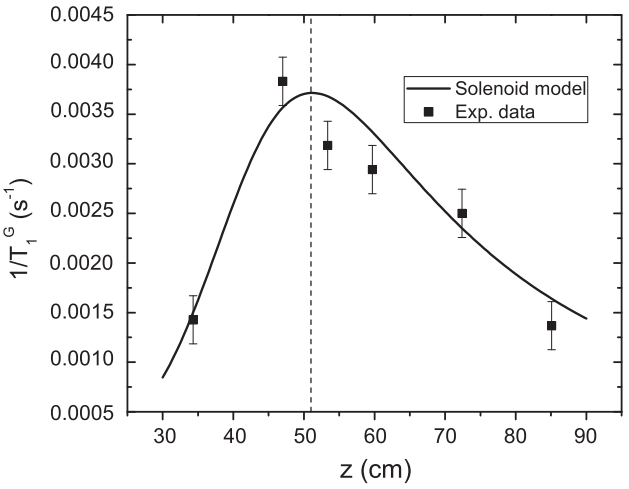

Fig. 2. Longitudinal relaxation rate of HP ^{3}He at 1 atm as a function of position along the z-axis in the fringe field of the 2-T magnet. The solid curve is calculated from Eq. (5) based on modeling the magnet as a solenoid. The squares are the experimentally determined relaxation rate corrected by the retention factor and the wall relaxation rate $1/T_1^W$. The vertical dashed line is, where $1/T_1^G$ reaches a maximum based on the calculation. Gradient-induced relaxation dominates all other mechanisms and varies by more than 3-fold over a range of less than one meter.

to cause even faster relaxation. To simulate this effect, we take our 2-T magnet design and make it hypothetically self-shielded by adding another solenoid to our model with a larger radius. The current of the larger solenoid is reversed and adjusted, so that the dipole field from the outer solenoid cancels the dipole field from the inner solenoid [28]. The current of the inner solenoid is increased to retain a 2-T primary field on-axis. The parameters used for the reversed solenoid are also shown in Table 1. The calculated on-axis $1/T_1^G$ for the self-shielded solenoid is plotted in Fig. 3a, together with the unshielded one. The maximum relaxation rate is nearly 3-fold higher ($1.37 \times 10^{-3}\ s^{-1}$) for the shielded versus unshielded design ($3.71 \times 10^{-3}\ s^{-1}$). The point at which maximum relaxation occurs is also shifted slightly further out from the magnet center.

We have also calculated $1/T_1^G$ for a 1.5-T self-shielded clinical magnet (GE Healthcare, 60 cm bore). The current configuration of the clinical magnet is proprietary, but was provided to us so that its fringe field and associated $1/T_1^G$ could be computed exactly. For reference, we have also simulated this magnet using a simplified model based on two nested solenoids as discussed for the 2-T magnet. The parameters for the two solenoids used in the calculation are shown in Table 1. The calculated $1/T_1^G$ based on the solenoid model agrees well with that based on the exact current configuration and suggests the simple model is again adequate. For further comparison, we then "turn off" all the reversed current in the exact current configuration, to evaluate the magnet as if it were unshielded and calculate the associated $1/T_1^G$ as shown in Fig. 3b. The comparison shows the maximum $1/T_1^G$ to be 2-fold faster for the shielded ($1.4 \times 10^{-3}\ s^{-1}$) versus unshielded ($7.4 \times 10^{-3}\ s^{-1}$) design. The peak relaxation rate occurs about 120 cm from the magnet isocenter, and diminishes by an order of magnitude 400 cm from the isocenter. However, the maximum relaxation rate on the axis of a self-shielded clinical magnet is still an order of magnitude slower than that near the self-shielded 2-T small magnet.

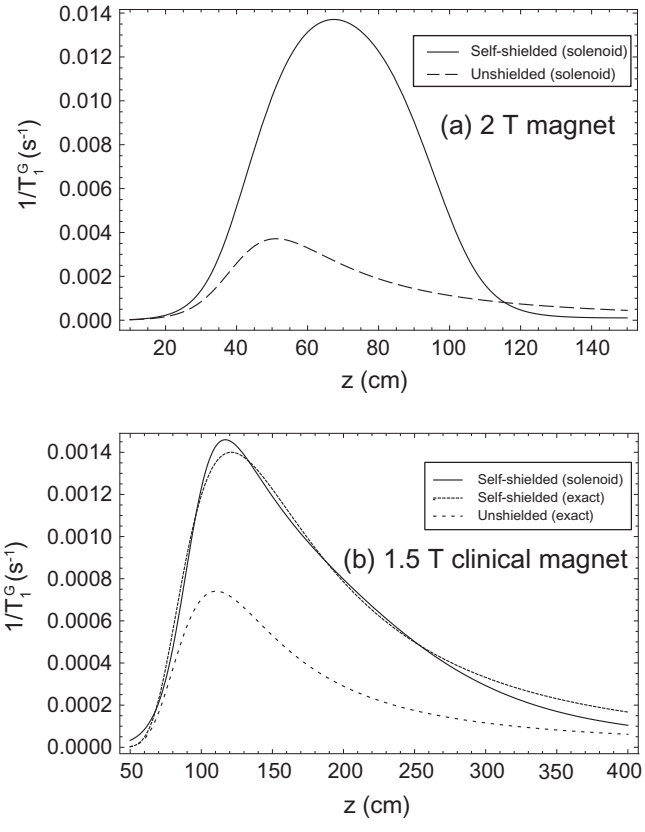

Fig. 3. The effect of a shielded magnet design on $1/T_1^G$ of HP ^{3}He is compared to an unshielded design. (a) 2-T medium-bore magnet. (b) 1.5-T clinical magnet. The solid lines are self-shielded solenoids and the dashed lines are unshielded solenoids. For the clinical 1.5-T magnet (b), the calculated $1/T_1^G$ is shown using both the exact current configuration provided by the manufacturer (dotted line) and a simplified representation based on two nested solenoids (solid line).

Some physical insight can be gained regarding the typical spatial dependence of $1/T_1^G$ by substituting the solenoid model Eq. (7) into Eq. (4). The resulting relaxation rate is given by

$$\frac{1}{T_1^G} \propto \frac{4R^4}{L^2}\left\{\frac{\frac{1}{[(1+2z/L)^2+(2R/L)]^{3/2}}-\frac{1}{[(1-2z/L)^2+(2R/L)^2]^{3/2}}}{\frac{1+2z/L}{[(1+2z/L)^2+(2R/L)^2]^{1/2}}+\frac{1-2z/L}{(1-2z/L)^2+(2R/L)^{1/2}}}\right\}^2. \tag{10}$$

Eq. (10) shows that $1/T_1^G$ is approximately proportional to $1/L^2$, and therefore suggests that the fringe field of a long magnet should generally cause slower relaxation. Moreover, Eq. (10) shows that for the case $2R/L \ll 1$, the gradient, and thus the relaxation rate, will be maximized at $z \approx \pm L/2$, which corresponds to the edges of the solenoid. For the less unusual case of $R \gg L$, numerical evaluation of Eq. (10) shows that the peak relaxation rate moves to $z \approx \pm R$.

To this point, our calculations and discussions have been limited to the on-axis relaxation rate and have shown that the theory and experiment agree well. Although most practical studies will store and deliver HP gas along the axis, it is useful to consider the degree to which relaxation increases away from the axis. The off-axis relaxation rate can be calculated using the more general near-axis approximation in Eq. (6). Using our unshielded 2-T magnet as an example, and setting ρ = 10 cm, while keeping z at 51 cm, where relaxation is maximum on-axis, the approximate solution gives a relaxation rate of $5.2 \times 10^{-3}\ s^{-1}$, which is 40% faster than the on-axis rate due to lack of symmetry. This rate continues to increase with ρ, but the approximation becomes less accurate, and Eq. (1) must be numerically evaluated using the exact field calculated from the Biot-Savart integration. Additionally, B_0 will no longer point along the z-direction, making the coordinate system defining the local field and the gradient components position-dependent. The calculated relaxation rate is shown in Fig. 4, and

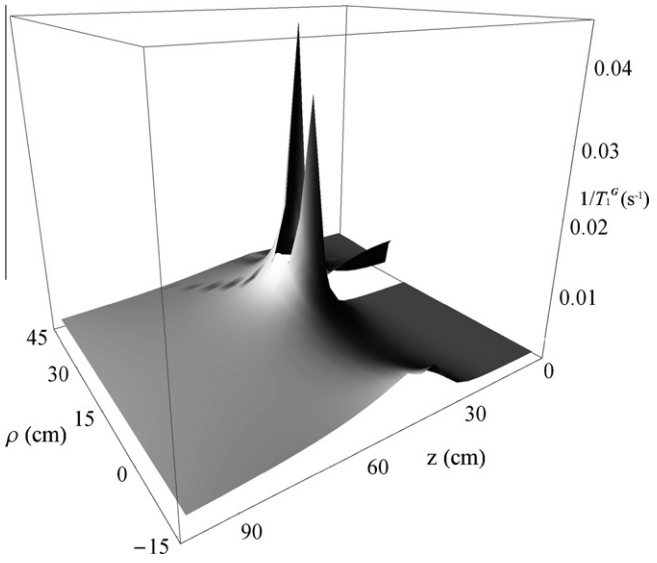

Fig. 4. Calculated $1/T_1^G$ of HP ^{3}He in the vicinity of the 2-T small bore magnet based on the solenoid model and the values stated in Table 1. The field is computed exactly by using Biot-Savart integration. Relaxation rates cannot be evaluated in the vicinity of the solenoid current loops ($\rho = 22$ cm, $|z| \leqslant 37.5$ cm) and therefore this part of the plot has been set to zero for clarity.

has the interesting feature that for any value of ρ, the maximum relaxation rate occurs at nearly the same value of z as the maximum on-axis rate. The relaxation rate increases rapidly with ρ, reaching $3.6 \times 10^{-2}\ s^{-1}$ ($\sim$28 s) at ρ = 20 cm, the largest radial distance for which a relaxation rate could be reliably calculated. As expected, once ρ exceeds the radius of the solenoid in the model, the relaxation rate begins to decrease. Hence, this numerical evaluation shows that $1/T_1^G$ is likely to be a maximum at the edge of the solenoid ($\rho \sim R$) and can exceed the peak relaxation rate observed on-axis by nearly an order of magnitude.

Finally, note that the gradients are directly proportional to the field strength. Thus, Eq. (1) indicates that the relaxation rates do not depend on B_0, but rather only on the particular geometry of the current configuration of the magnet. Hence, the calculations we have done for our 2-T, small animal imaging magnet should be equally applicable to a 4.7-T or 7-T system of similar geometry, and those for the 1.5-T clinical magnet would be equally applicable at 3-T.

While we have not reported direct measurements for ^{129}Xe, it can reasonably be surmised that gradient-induced relaxation rate will be $\sim$35-times slower than that observed for ^{3}He. This large difference arises from the substantially smaller free diffusion coefficient [29] of $5.71 \times 10^{-2}\ cm^2/s$ for ^{129}Xe compared to ^{3}He ($2.0\ cm^2/s$). Thus, gradient relaxation should be considered for ^{129}Xe, but it is unlikely to be as significant a problem as for ^{3}He. For instance, the worst "spot" in the on-axis fringe field of the 2-T small bore magnet gives a relaxation time about 140 min for ^{129}Xe, which is on the same order as the relaxation time due to the wall relaxation.

5. Conclusion

We have shown that the minimum relaxation time for ^{3}He in the vicinity of an unshielded small bore MR system can be as short as 4 min on-axis and is reduced to 0.5 min, when moving out 20 cm in the radial direction. Moreover, the minimum on-axis ^{3}He relaxation time would drop to roughly 1.2 min, if the magnet were self-shielded. Gradient-induced relaxation in a typical self-shielded clinical magnet is less severe, but still significant and is expected to contribute a minimum on-axis ^{3}He relaxation time of roughly 12 min. We have also shown that the cylindrical symmetry of most magnet systems enables the off-axis fringe field to be predicted simply by measuring the on-axis field. Moreover, any model that adequately captures the behavior of the fringe field can be used to calculate the gradient-induced longitudinal relaxation. We have shown for the cases considered here, that a simple solenoid model is adequate. Taken together, these results provide a general approach for predicting the gradient-induced relaxation rate and the position, where this rate is maximized. This information, in turn, provides a means of maximizing the lifetime of HP gases stored within the fringe field of most superconducting magnet systems.

Acknowledgments

The authors wish to thank Sally Zimney for carefully proofreading the manuscript. This work was conducted at the Duke Center for In Vivo Microscopy, an NIH/NCRR National Biomedical Technology Research Center (P41 RR005959) with further support from NCI (R01 CA142842).

Appendix A. Transformation of the rate equation into cylindrical coordinates

In cylindrical coordinates the gradient of B_x is given by $\nabla B_x = \frac{\partial B_x}{\partial \rho}\hat{\rho} + \frac{1}{\rho}\frac{\partial B_x}{\partial \phi}\hat{\phi} + \frac{\partial B_x}{\partial z}\hat{z}$. Therefore

$$|\vec{\nabla} B_x|^2 + |\vec{\nabla} B_y|^2 = \left(\frac{\partial B_x}{\partial \rho}\right)^2 + \left(\frac{1}{\rho}\frac{\partial B_x}{\partial \phi}\right)^2 + \left(\frac{\partial B_x}{\partial z}\right)^2 + \left(\frac{\partial B_y}{\partial \rho}\right)^2 + \left(\frac{1}{\rho}\frac{\partial B_y}{\partial \phi}\right)^2 + \left(\frac{\partial B_y}{\partial z}\right)^2. \tag{A1.1}$$

To evaluate this expression, we express B_x and B_y in cylindrical coordinates as $B_x = B_\rho \cos\phi - B_\phi \sin\phi$ and $B_y = B_\rho \sin\phi + B_\phi \cos\phi$, where ϕ is the polar angle and ρ is the radial component. However, for the case of a solenoid, which has no azimuthal component of magnetic field (B_ϕ = 0) we have simply, $B_x = B_\rho \cos\phi$ and $B_y = B_\rho \sin\phi$. Substituting these into Eq. (A1.1) gives sum of transverse gradients as

$$\begin{aligned}|\vec{\nabla} B_x|^2 + |\vec{\nabla} B_y|^2 &= \left(\frac{\partial(B_\rho \cos\phi)}{\partial \rho}\right)^2 + \left(\frac{1}{\rho}\frac{\partial(B_\rho \cos\phi)}{\partial \phi}\right)^2 + \left(\frac{\partial(B_\rho \cos\phi)^2}{\partial z}\right) + \left(\frac{1}{\rho}\frac{\partial(B_\rho \sin\phi)}{\partial \rho}\right)^2 + \left(\frac{1}{\rho}\frac{\partial(B_\rho \sin\phi)}{\partial \phi}\right)^2 + \left(\frac{1}{\rho}\frac{\partial(B_\rho \sin\phi)}{\partial Z}\right)^2 \\ &= \left(\frac{\partial B_\rho}{\partial \rho}\right)^2 + \left(\frac{1}{\rho}\frac{\partial B_\rho}{\partial \phi}\right)^2 + \left(\frac{\partial B_\rho}{\partial z}\right)^2 + \frac{B_\rho^2}{\rho^2} \\ &= |\vec{\nabla} B_\rho|^2 + \frac{B_\rho^2}{\rho^2}.\end{aligned} \tag{A1.2}$$

Appendix B. Off-axis approximations

To relate $B_z(\rho, z)$ and $B_\rho(\rho, z)$, it is first necessary to expanded these functions in Taylor series in terms of ρ as

$$\begin{aligned}B_z(\rho, z) &= B_z(0, z) + \rho\frac{\partial}{\partial \rho}B_z(0, z) + \frac{\rho^2}{2!}\frac{\partial^2}{\partial \rho^2}B_z(0, z) + \cdots \\ &= \sum_{n=0}^{\infty}\frac{\rho^n}{n!}B_z^{(n)}(0, z),\end{aligned} \tag{A2.1a}$$

$$\begin{aligned}B_\rho(\rho, z) &= B_\rho(0, z) + \rho\frac{\partial}{\partial \rho}B_\rho(0, z) + \frac{\rho^2}{2!}\frac{\partial^2}{\partial \rho^2}B_\rho(0, z) + \cdots \\ &= \sum_{n=0}^{\infty}\frac{\rho^n}{n!}B_\rho^{(n)}(0, z),\end{aligned} \tag{A2.1b}$$

where $B_z^{(n)}$ and $B_\rho^{(n)}$ are the nth derivative of B_z and B_ρ with respect to ρ. Since the magnetic field is divergence-free, the relationship between B_z and B_ρ is given by

$$\vec{\nabla} \bullet \vec{B} = \frac{1}{\rho}\frac{\partial}{\partial \rho}(\rho B_\rho) + \frac{\partial}{\partial z}B_z = 0. \tag{A2.2}$$

This relatively truncated expression arises because B_ϕ = 0 and B_ρ and B_z do not depend on ϕ. Substituting Eqs. (A2.1a) and (A2.1b) into Eq. (A2.2) yields

$$\frac{1}{\rho}B_\rho^{(0)}(0, z) + \sum_{n=0}^{\infty}\rho^n\left[\frac{n+2}{(n+1)!}B_\rho^{(n+1)}(0, z) + \frac{1}{n!}\frac{\partial}{\partial z}B_z^{(n)}(0, z)\right] = 0. \tag{A2.3}$$

Since Eq. (A2.3) must hold for any value of ρ, $B_\rho^{(0)}(0, z) = 0$ and every term in the summation must be zero as well. Therefore the terms within the summation can be used to relate $B_\rho^{(n)}(0, z)$ to $B_z^{(n)}(0, z)$ by the equality

$$\frac{-n+2}{n+1}B_\rho^{(n+1)}(0, z) = \frac{1}{\partial z}B_z^{(n)}(0, z). \tag{A2.4}$$

Because no current is present near the central axis of the magnet, the magnetic field $\vec{B}$ must also be curl-free. For any magnet having a symmetric current only in the $\hat{\phi}$ direction, this leaves the only non-trivial term in the curl equation to be the $\hat{\phi}$ component. Hence,

$$\begin{aligned}\vec{\nabla}\times\vec{B} &= \left(\frac{\partial B_\rho}{\partial z}-\frac{\partial B_z}{\partial \rho}\right)\hat{\phi}\\ &= \left\{\sum_{n=0}^{\infty}\frac{\rho^n}{n!}\frac{\partial}{\partial z}B_\rho^{(n)}(0,z)-\sum_{n=1}^{\infty}\frac{\rho^{n-1}}{(n-1)!}B_z^{(n)}(0,z)\right\}\hat{\phi}\\ &= \left\{\sum_{n=0}^{\infty}\frac{\rho^n}{n!}\left[\frac{\partial}{\partial z}B_\rho^{(n)}(0,z)-B_z^{(n+1)}(0,z)\right]\right\}\hat{\phi}=0. \end{aligned} \tag{A2.5}$$

Eq. (A2.5) provides an additional relationship between the derivatives $B_\rho^{(n)}(0,z)$ and $B_z^{(n)}(0,z)$, namely

$$\frac{\partial}{\partial z}B_\rho^{(n-1)}(0,z)=B_z^{(n)}(0,z). \tag{A2.6}$$

Combining Eqs. (A2.4) and (A2.6) yields a recursion equation for $B_\rho^{(n)}(0,z)$ with the form

$$\frac{\partial^2}{\partial z^2}B_\rho^{(n)}(0,z)=-\frac{n+3}{n+2}B_\rho^{(n+2)}(0,z). \tag{A2.7}$$

Since, as described previously, $B_\rho^{(0)}(0,z)=0$, this recursion relation requires all even terms to vanish, leaving only the odd terms ($n=2k+1$). Therefore, these terms can be written as

$$B_\rho^{(2k+1)}(0,z)=\frac{(-1)^k}{2^{2k}}\frac{(2k+1)!}{(2k+2)(k!)^2}\frac{\partial^{2k+1}}{\partial z^{2k+1}}B_z^{(0)}(0,z)\quad(k=0,1,2,\ldots), \tag{A2.8}$$

where Eq. (A2.4) has been used to express $B_\rho^{(1)}(0,z)$ in terms of $B_z^{(0)}(0,z)$. As $B_z^{(n)}(0,z)$ is related to $B_\rho^{(n-1)}(0,z)$ through Eq. (A2.6), all the even terms ($n=2k$) of $B_z^{(n)}(0,z)$ are non-zero and they can be expressed as

$$B_z^{(2k)}(0,z)=\frac{(-1)^k}{2^{2k}}\frac{(2k)!}{(k!)^2}\frac{\partial^{2k}}{\partial z^{2k}}B_z^{(0)}(0,z)\quad(k=0,1,2\ldots). \tag{A2.9}$$

By substituting Eqs. (A2.8) and (A2.9) into Eq. (A2), both $B_z(\rho,z)$ and $B_\rho(\rho,z)$ can be expressed in terms of $B_z(0,z)$ and its higher-order derivatives as

$$B_z(\rho,z)=\sum_{k=0}^{\infty}\frac{(-)^k}{(k!)^2 4^k}\rho^{2k}\frac{\partial^{2k}}{\partial z^{2k}}B_z^{(0)}(0,z), \tag{A2.10a}$$

$$B_\rho(\rho,z)=\sum_{k=0}^{\infty}\frac{(-1)^{k+1}}{(2k+2)(k!)^2 4^k}\rho^{2k+1}\frac{\partial^{2k+1}}{\partial z^{2k+1}}B_z^{(0)}(0,z). \tag{A2.10b}$$

Note that this Taylor expansion converges when $\rho < R_0$, where R_0 is the smallest radius of the current distribution(s) constituting the magnet. If $B_z(0,z)$ varies slowly in space (i.e., $B_z^{(k+2)}(0,z)/B_z^{(k)}(0,z)\ll 1$), the expansion of B_z and B_ρ will converge quickly and consequently, it is sufficient to truncate the series expansion in Eqs. (A2.10a) and (A2.10b) at the second term, which leads to

$$B_z(\rho,z)\simeq B_z(0,z)-\frac{\rho^2}{4}\frac{\partial^2}{\partial z^2}B_z(0,z), \tag{A2.11a}$$

$$B_\rho(\rho,z)\simeq -\frac{\rho}{2}\frac{\partial}{\partial z}B_z(0,z)+\frac{\rho^3}{16}\frac{\partial^3}{\partial z^3}B_z(0,z). \tag{A2.11b}$$

References

[1] H.E. Moller, X.J. Chen, B. Saam, K.D. Hagspiel, G.A. Johnson, T.A. Altes, E.E. de Lange, H.U. Kauczor, Magnetic Resonance in Medicine 47 (2002) 1029–1051.
[2] L. Schroder, T.J. Lowery, C. Hilty, D.E. Wemmer, A. Pines, Molecular imaging using a targeted magnetic resonance hyperpolarized biosensor, Science 314 (2006) 446–449.
[3] I.A. Nelson, B. Chann, T.G. Walker, Spin-exchange optical pumping using a frequency-narrowed high power diode laser, Applied Physics Letters 76 (2000) 1356–1358.
[4] E. Babcock, I. Nelson, S. Kadlecek, B. Driehuys, L.W. Anderson, F.W. Hersman, T.G. Walker, Hybrid spin-exchange optical pumping of He-3, Physical Review Letters 91 (2003) 123003.
[5] W.C. Chen, T.R. Gentile, T.G. Walker, E. Babcock, Spin-exchange optical pumping of He-3 with Rb–K mixtures and pure K, Physical Review A 75 (2007) 013416.
[6] I.C. Ruset, S. Ketel, F.W. Hersman, Optical pumping system design for large production of hyperpolarized, Physical Review Letters 96 (2006) 053002.
[7] E. Babcock, B. Chann, T.G. Walker, W.C. Chen, T.R. Gentile, Limits to the polarization for spin-exchange optical pumping of He-3, Physical Review Letters 96 (2006) 083003.
[8] M.L. Smith, C. Dybowski, NMR spin-lattice relaxation of Xenon adsorbed in Na–Y zeolite, Journal of Physical Chemistry 95 (1991) 4942–4944.
[9] N.R. Newbury, A.S. Barton, G.D. Cates, W. Happer, H. Middleton, Gaseous He-3–He-3 magnetic dipolar spin relaxation, Physical Review A 48 (1993) 4411–4420.
[10] H.C. Torrey, Chemical shift and relaxation of Xe-129 in xenon gas, Physical Review 130 (1963) 2306–2312.
[11] I.L. Moudrakovski, S.R. Breeze, B. Simard, C.I. Ratcliffe, J.A. Ripmeester, T. Seideman, J.S. Tse, G. Santyr, Gas-phase nuclear magnetic relaxation in Xe-129 revisited, Journal of Chemical Physics 114 (2001) 2173–2181.
[12] B.N. Berry-Pusey, B.C. Anger, G. Laicher, B. Saam, Nuclear spin relaxation of Xe-129 due to persistent xenon dimers, Physical Review A 74 (2006) 063408.
[13] B. Chann, I.A. Nelson, L.W. Anderson, B. Driehuys, T.G. Walker, Xe-129–Xe molecular spin relaxation, Physical Review Letters 88 (2002) 113201.
[14] C.J. Jameson, A.K. Jameson, J.K. Hwang, Nuclear-spin relaxation by intermolecular magnetic dipole coupling in the gas-phase–Xe-129 in oxygen, Journal of Chemical Physics 89 (1988) 4074–4081.
[15] B. Saam, W. Happer, H. Middleton, Nuclear relaxation of He-3 in the presence of O_2, Phys. Rev. A 52 (1995) 862–865.
[16] G.D. Cates, S.R. Schaefer, W. Happer, Relaxation of spins due to field inhomogeneities in gaseous samples at low magnetic-fields and low-pressures, Physical Review A 37 (1988) 2877–2885.
[17] G.E. Santyr, W.W. Lam, J.M. Parra-Robles, T.M. Taves, A.V. Ouriadov, Hyperpolarized noble gas magnetic resonance imaging of the animal lung: approaches and applications, Journal of Applied Physics 105 (2009) 102004.
[18] E.J.R. van Beek, J. Schmiedeskamp, J.M. Wild, M.N.J. Paley, F. Filbir, S. Fichele, F. Knitz, G.H. Mills, N. Woodhouse, A. Swift, W. Heil, M. Wolf, E. Otten, Hyperpolarized 3-Helium MR imaging of the lungs: testing the concept of a central production facility, European Radiology 13 (2003) 2583–2586.
[19] B.C. Anger, G. Schrank, A. Schoeck, K.A. Butler, M.S. Solum, R.J. Pugmire, B. Saam, Gas-phase spin relaxation of Xe-129, Physical Review A 78 (2008) 043406.
[20] J.W. McIver, R. Erwin, W.C. Chen, T.R. Gentile, End-compensated magnetostatic cavity for polarized He-3 neutron spin filters, Review of Scientific Instruments 80 (2009) 063905.
[21] A.C. Thomas, E.N. Potts, B.T. Chen, D.M. Slipetz, W.M. Foster, B. Driehuys, A robust protocol for regional evaluation of methacholine challenge in mouse models of allergic asthma using hyperpolarized He-3 MRI, Nmr in Biomedicine 22 (2009) 502–515.
[22] H.E. Moller, X.J. Chen, M.S. Chawla, B. Driehuys, L.W. Hedlund, G.A. Johnson, Signal dynamics in magnetic resonance imaging of the lung with hyperpolarized noble gases, Journal of Magnetic Resonance 135 (1998) 133–143.
[23] A.J. Deninger, S. Mansson, J.S. Petersson, G. Pettersson, P. Magnusson, J. Svensson, B. Fridlund, G. Hansson, I. Erjefeldt, P. Wollmer, K. Golman, Quantitative measurement of regional lung ventilation using He-3 MRI, Magnetic Resonance in Medicine 48 (2002) 223–232.
[24] R.L. Gamblin, T.R. Carver, Polarization and relaxation processes in He-3 gas, Physical Review 138 (1965) A946–A960.
[25] L.D. Schearer, G.K. Walters, Nuclear spin-lattice relaxation in the presence of magnetic-field gradients, Physical Review 139 (1965) A1398–A1402.
[26] T.G. Walker, W. Happer, Spin-exchange optical pumping of noble-gas nuclei, Review of Modern Physics 69 (1997) 629–642.
[27] I. Nelson, B. Driehuys, S. Kadlecek, Remote calibration of accurate hyperpolarized gas polarimetry, in: 12th Annual Scientific Meeting, ISMRM 2004, pp. 1689.
[28] A.K. Kalafala, A design approach for actively shielded magnetic-resonance-imaging magnets, IEEE Transactions on Magnetics 26 (1990) 1181–1188.
[29] R.W. Mair, D.G. Cory, S. Peled, C.H. Tseng, S. Patz, R.L. Walsworth, Pulsed-field-gradient measurements of time-dependent gas diffusion, Journal of Magnetic Resonance 135 (1998) 478–486.